



Article

Computational Modeling and Imaging of the Intracellular Oxygen Gradient

Andrew J. H. Sedlack ¹, Rozhin Penjweini ², Katie A. Link ², Alexandra Brown ³, Jeonghan Kim ^{3,4}, Sung-Jun Park ³, Jay H. Chung ³, Nicole Y. Morgan ¹ and Jay R. Knutson ^{2,*}

¹ Biomedical Engineering and Physical Science Shared Resource, National Institute of Biomedical Imaging and Bioengineering (NIBIB), National Institutes of Health (NIH), Bethesda, MD 20892-5766, USA

² Laboratory of Advanced Microscopy and Biophotonics, National Heart, Lung, and Blood Institute (NHLBI), National Institutes of Health (NIH), Bethesda, MD 20892-1412, USA

³ Laboratory of Obesity and Aging Research, National Heart, Lung, and Blood Institute (NHLBI), National Institutes of Health (NIH), Bethesda, MD 20892-1412, USA

⁴ Department of Biochemistry, College of Medicine, The Catholic University of Korea, Seoul 06591, Korea

* Correspondence: knutsonj@nhlbi.nih.gov; Tel.: +1-301-496-2557; Fax: +1-301-480-6964

Abstract: Computational modeling can provide a mechanistic and quantitative framework for describing intracellular spatial heterogeneity of solutes such as oxygen partial pressure (pO_2). This study develops and evaluates a finite-element model of oxygen-consuming mitochondrial bioenergetics using the COMSOL Multiphysics program. The model derives steady-state oxygen (O_2) distributions from Fickian diffusion and Michaelis–Menten consumption kinetics in the mitochondria and cytoplasm. Intrinsic model parameters such as diffusivity and maximum consumption rate were estimated from previously published values for isolated and intact mitochondria. The model was compared with experimental data collected for the intracellular and mitochondrial pO_2 levels in human cervical cancer cells (HeLa) in different respiratory states and under different levels of imposed pO_2 . Experimental pO_2 gradients were measured using lifetime imaging of a Förster resonance energy transfer (FRET)-based O_2 sensor, Myoglobin-mCherry, which offers in situ real-time and noninvasive measurements of subcellular pO_2 in living cells. On the basis of these results, the model qualitatively predicted (1) the integrated experimental data from mitochondria under diverse experimental conditions, and (2) the impact of changes in one or more mitochondrial processes on overall bioenergetics.

Keywords: myoglobin-mCherry; mitochondrial pO_2 gradient; finite-element analysis



Citation: Sedlack, A.J.H.; Penjweini, R.; Link, K.A.; Brown, A.; Kim, J.; Park, S.-J.; Chung, J.H.; Morgan, N.Y.; Knutson, J.R. Computational Modeling and Imaging of the Intracellular Oxygen Gradient. *Int. J. Mol. Sci.* **2022**, *23*, 12597. <https://doi.org/10.3390/ijms232012597>

Academic Editors: Joseph P. Albanesi and David M. Jameson

Received: 5 September 2022

Accepted: 17 October 2022

Published: 20 October 2022

Publisher's Note: MDPI stays neutral with regard to jurisdictional claims in published maps and institutional affiliations.



Copyright: © 2022 by the authors. Licensee MDPI, Basel, Switzerland. This article is an open access article distributed under the terms and conditions of the Creative Commons Attribution (CC BY) license (<https://creativecommons.org/licenses/by/4.0/>).

1. Introduction

It is widely recognized that intracellular oxygen partial pressure (pO_2) plays an important role in cellular function and metabolism. In most functioning cells, the oxygen (O_2) level needs to be sufficient to maintain mitochondrial activity, providing adenosine triphosphate (ATP) and other substances essential for normal cell function [1,2]. Despite broad consensus on the importance of O_2 concentration ($[O_2]$), many important quantitative aspects of the physiological and pathophysiological phenomena related to pO_2 remain unclear. This is due, in part, to a lack of methodology to make accurate measurements of intracellular and subcellular pO_2 .

In extant experimental and theoretical work involving the role of pO_2 , the values used are frequently imposed extracellular pO_2 , because those values can be more readily measured. This approach is based on the assumption that there are no steep pO_2 gradients in or around cells. While there is ample computational and experimental precedent stating that sharp gradients over the span of a few microns are unlikely, regional gradients within and around cells have been measured, and their presence is supported by some models [3–6]. The mechanism of these pO_2 gradients, however, remains uncertain due to several untested

key assumptions. The role of lipid bilayers (such as the cell membrane and intracellular compartmental membranes) as barriers to gas diffusion is highly controversial, with varying results having been measured or computed depending on the precise composition of the membrane [3,7–11].

Early modelers predicted that regional O₂ gradients across or within cells were not possible within diffusion-dominated regimes [4,12]. These models continue to be cited as evidence that there are limited, if any, intracellular O₂ gradients. Significantly, these models only considered O₂ gradients arising outside a mitochondrion or cell sitting in a 3D O₂ permeable volume, such as a cell suspension or within permeable tissue; the geometry used for adherent tissue culture, in which cells sit on an O₂-impermeable substrate, was not considered [13–15].

While early modeling results led to a reconsideration of then-available measurement techniques, significant O₂ gradients across cells have continued to be observed from electron paramagnetic resonance (EPR) spectroscopy and more modern phosphorescence and fluorescence lifetime and intensity-based imaging (using either a microplate reader or a microscope) [6,16–19]. Some studies showed significant intracellular gradients purely on the basis of differences in mean compartmental average values rather than imaging across whole cells [5,20]. The modeling of local gradients formed on length scales comparable to the subcellular structure of mitochondrial organization is made more tractable with finite-element methods. This recently enabled full-cell bioenergetic finite-element models of mitochondrial O₂ consumption in cardiomyocytes, which showed gradients as steep as 2 Torr/ μm [21,22]. We now present a model for subcellular O₂ concentration and consumption under common in vitro conditions to better complement current imaging and measurement techniques.

Most recently, we used fluorescence lifetime imaging (FLIM) of a Förster resonance energy transfer (FRET)-based sensor, Myoglobin (Myo)-mCherry, with targeting sequences attached that enabled us to measure pO₂ within the mitochondria and cytosol, finding differences of up to 11 mmHg between the compartments under some conditions [23,24]. Using microscopic images of mitochondria in C2C12 mouse myoblast cells, we developed a model that incorporated an extended, spatially complex mitochondrial compartment in which O₂ consumption is governed by Michaelis–Menten kinetics, and we looked at the resulting gradients in subcellular [O₂] in and around this compartment. Looking at a range of experimental conditions and consensus values from the literature for O₂ diffusion, solubility, and consumption, we saw qualitative agreement between the computational model and experimental measurements of the differences (0.4, 1, 3, and 4 mmHg at applied [O₂] of 0.5%, 5%, 10%, and 18.5%, respectively) between the intracellular and mitochondrial compartments in a human cervical cancer cell line (HeLa).

2. Results

2.1. Measurements of the Intracellular pO₂ Gradients

In tissue culture of adherent cells, the balance between mitochondrial O₂ consumption of the cell monolayer at the bottom of the petri dish and the primarily diffusive transport of O₂ through media is a major determinant of pericellular O₂. For dense layers of metabolically active cells, pericellular pO₂ can drop quite low, even in ambient atmospheric [O₂]. Cells with low or non-consuming mitochondria, on the other hand, are likely to experience greater intracellular pO₂ than those more rapidly consuming O₂ [25].

Figure 1a shows intracellular and mitochondrial pO₂ at different values of imposed pO₂, as measured using lifetime imaging of Myo-mCherry and mitochondrial-targeted Myo-mCherry (mtMyo-mCherry) and a calibration curve derived from non-respiring (rotenone/antimycin-treated) cells. The differences between the average lifetime values obtained for the non-respiring cells transfected with Myo-mCherry or mtMyo-mCherry were not statistically significant; the data shown for non-respiring cells in Figure 1a are for cells transfected with Myo-mCherry. Here, we use imposed pO₂ to mean the extracellular [O₂] measured using the OxyLite Pro device; this fiber probe quantifies pO₂ in the medium,

approximately 100 microns above the cell layer. The lifetime data were fitted using the hyperbolic equation Equation (1) (see Section 4.6); fitting parameters are available in Table 1. Rearranging Equation (1) and using the values of K and τ_{max} obtained for the rotenone/antimycin-treated cells, we obtained a calibration curve relating the lifetime of the Myo-mCherry probes to pO_2 . Using this calibration, we calculate the effective pO_2 for each subcellular compartment in respiring cells from the lifetime data, and we plot it as a function of imposed pO_2 in Figure 1b. Pseudocolor mapping examples of pO_2 in the intracellular and mitochondrial environments at normoxia and hypoxia are plotted in Figure 1c,d, respectively. More detailed descriptions of the pO_2 mapping procedure can be found in Ref. [23].

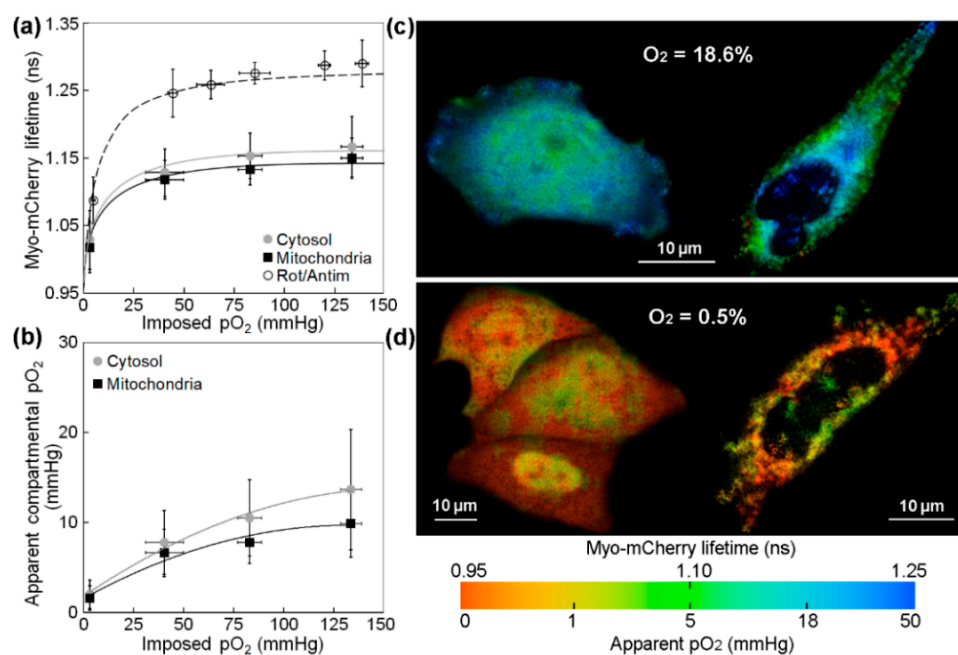


Figure 1. (a) Average fluorescence lifetime of Myo-mCherry in the cytosol and mitochondria of respiring and non-respiring (rotenone/antimycin treated) HeLa cells plotted versus medium pO_2 values obtained from OxyLite Pro measurements; the data are shown with the best hyperbolic fit obtained from Equation (1). (b) The apparent intracellular pO_2 versus the medium imposed pO_2 ; error bars are the standard deviations. Pseudocolor mapping of Myo-mCherry lifetime (or pO_2) in the cytosol (left) and mitochondria (right) of HeLa cells at atmospheric pO_2 of (c) 18.6% and (d) 0.5%. In the color bars, red indicates lower lifetime and pO_2 values, whereas blue indicates higher values.

Table 1. Parameters of the hyperbolic fits. Parameter K was obtained from fitting the data presented in Figure 1a to Equation (1). τ_{max} is the longest average lifetime for Myo-mCherry measured at $O_2 = 18.6\%$. The imposed pO_2 values were obtained from the OxyLite Pro fiber tip measurements.

	OxyLite Pro		
	τ_{max}	K	R^2
Mitochondria	1.15 ± 0.03	6.889 ± 2.819	0.99
Cytosol	1.17 ± 0.04	6.852 ± 3.498	0.98
Rot/Antim	1.29 ± 0.03	6.764 ± 1.577	0.98

By examining a variety of anoxic through normoxic conditions, one can see that the intracellular versus imposed pO_2 trends are similar and hyperbolic for all cell compartments. Clearly, the sustained intracellular pO_2 levels, well below those applied, reflect O_2 consumption in HeLa cells. For the highest atmospheric $[O_2]$ used here (18.6%, or

about 140 mmHg), we see apparent intracellular pO_2 levels of 14 mmHg in the cytosol and 10 mmHg in the mitochondria.

Note that the medium-imposed pO_2 measured with the OxyLite is assumed to be identical to that in the intracellular volume only for the non-respiring cells; these values are clearly different for cells with active mitochondrial respiration. The myoglobin saturation-controlled lifetime values still represent in situ metabolic pO_2 . In other words, the affinity for O_2 of the myoglobin in the chimeric probe defines the relationship between lifetime and local pO_2 . The only assumption in this back-calculation mapping is that rotenone/antimycin joint treatment effectively equalizes medium-imposed and internal local levels.

2.2. COMSOL Modeling of the Intracellular pO_2 Gradients

We modeled $[O_2]$ at equilibrium in the diffusion-dominated regime surrounding cells grown in monolayer culture. As shown in Figure 2, we used a symmetric model representative of a uniform square grid of cells, specifically, a periodic boundary condition using one-quarter of a single cell in a rectangular column of medium with symmetric (i.e., zero flux) lateral boundaries. Mitochondrial structure for the model was scanned from a C2C12 mouse myoblast cell (see Figure S1 in Supplementary Materials) in order to provide insight into the possible impact of the spatial structure and organization of the mitochondrial volume on subcellular O_2 gradients. We adjusted the edge length of the medium column (i.e., distance between cells) to represent different cellular densities (i.e., confluence level), and a constant applied $[O_2]$ was assumed at the top boundary.

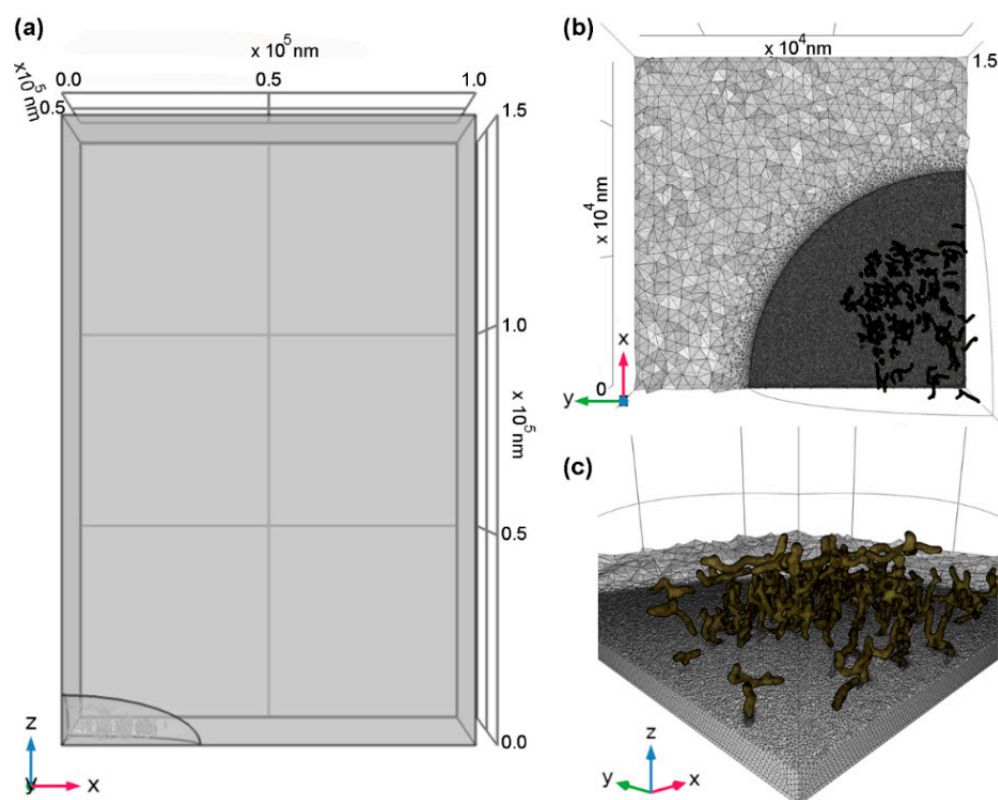


Figure 2. (a) Model geometry viewed in profile; (b) cross-section of mesh viewed from above and (c) center. Rectangular volume defines a column of medium with eighth section of an ellipsoid defining the cytoplasm and live-cell imaged mitochondrial geometry (in gold for meshes). Boundary conditions are as described in Section 4.

The equilibrium intracellular pO_2 gradients were calculated for a range of applied $[O_2]$, cell spacings, and lower boundary conditions. Models were also generated for different

maximal mitochondrial O₂ consumption rates and diffusion conditions; however, in the end, only the highest consumption rate seen in the literature and consensus diffusion constants were used here. The resulting calculations for mean pO₂ in mitochondrial and cytosolic compartments are presented in Table 2. Alternatively, minimal mitochondrial and maximal cytoplasmic values are presented in Supplementary Table S1 in order to show the maximal difference observed between compartments.

Table 2. Mean pO₂ in mitochondrial and cytosolic cellular compartments for models with different applied O₂ concentrations, cell spacings, and lower boundary conditions. Spacing describes the distance from the center of one cell to the center of the next cell in the square grid approximation of a monolayer.

O ₂ (%)	Spacing (μm)	Lower Boundary	Mean Mitochondrial pO ₂ (mmHg)	Mean Cytosolic pO ₂ (mmHg)	Difference (mmHg)
0.5	70	Glass	0.01	0.23	0.21
5			4.63	7.09	2.46
10			42.1	44.6	2.50
20			118.1	120.6	2.50
0.5	100	Glass	0.028	0.428	0.4
5			19.0	21.4	2.4
10			56.9	59.4	2.5
20			132.9	135.4	2.5
0.5	200	Glass	0.064	0.764	0.7
5			25.7	28.3	2.6
10			63.6	66.3	2.7
20			139.6	142.3	2.7
0.5	70	Ibidi Polymer	0.01	0.27	0.25
5			5.22	7.68	2.46
10			42.6	45.1	2.49
20			118.2	120.7	2.5
0.5	100	Ibidi Polymer	0.036	0.508	0.5
5			19.6	22.1	2.5
10			57.4	59.8	2.5
20			133.0	135.5	2.5
0.5	200	Ibidi Polymer	0.087	0.914	0.8
5			26.2	28.8	2.6
10			64.0	66.7	2.7
20			139.7	142.3	2.7
0.5	70	200 μm PDMS	0.38	1.27	0.89
5			33.2	34.5	1.31
10			71.2	72.5	1.32
20			147.2	148.5	1.32
0.5	100	200 μm PDMS	0.779	1.87	1.1
5			34.5	35.8	1.3
10			72.6	73.8	1.3
20			148.5	149.8	1.3
0.5	200	200 μm PDMS	1.08	2.30	1.2
5			35.0	36.4	1.4
10			73.0	74.4	1.4
20			149.0	150.4	1.4

As in the experimental measurements on substrates with low O₂ permeability, the difference between the mitochondrial and cytosolic compartments is significantly smaller at the lowest values for extracellular pO₂. At higher (5–20%) applied O₂ concentrations, the maximal difference is 2.4–2.7 mmHg for the cells plated on glass or Ibidi polymer

coverslips, similar to the differences seen experimentally with FLIM-FRET in Figure 1. However, the calculated values for intracellular O_2 concentrations are substantially higher than expected if we assume the $[O_2]$ at the top of the model volume is identical to the imposed O_2 measured with the OxyLite Pro. Looking at the model results for 10% applied O_2 and cells growing on glass with a 70 μm spacing, we see cytoplasmic $[O_2]$ of 44.6 mmHg in the model, compared to 10.5 mmHg found for the 10% imposed O_2 point in Figure 1b.

Slices showing pO_2 gradients at equilibrium for 100 μm cell–cell spacing are presented in Figure 3. At lower applied O_2 concentrations, pericellular levels drop below the K_M of mitochondrial consumption (0.078 mmHg), and diffusion cannot replace O_2 as rapidly as it is being consumed by mitochondria, giving rise to a region of relatively uniform hypoxia around the mitochondria. At higher applied O_2 levels, there is a greater amount of O_2 available in adjacent regions to replenish the consuming regions; hence, the gradient does not ‘bottom out’ in this way.

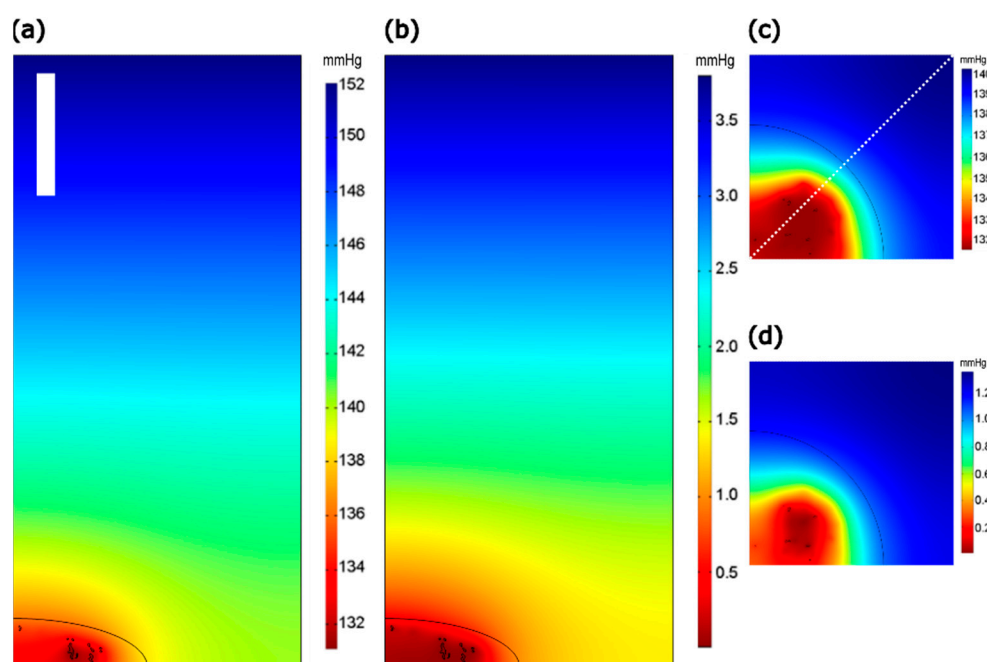


Figure 3. The pO_2 (mmHg) slices of model with 100 μm cell–cell spacing and glass lower boundary at equilibrium with applied pO_2 of (a,c) 20% and (b,d) 0.5%. (a,b) Planes through $y = x$ (i.e., diagonal to the square grid, in order to show longer dimension—shown as dotted line in panel (c)) and (c,d) xy planes through $z = 1 \mu m$. Color scales are fitted to individual panel ranges. All panels are the same geometric scale; the scalebar in (a) is 30 μm .

Figure 4a–c compare O_2 gradients in models with varying cell densities. Center-to-center cell spacings of 70, 100, and 200 μm correspond to cell seeding densities of 2.4×10^4 , 1×10^4 , 2.5×10^3 , and 1.1×10^3 cells/cm². At cell spacings at or beyond 200 μm , O_2 levels at the substrate in between cells reached those at the top surface of the computational volume 150 μm above the cell substrate, as expected. At cell spacings less than 200 μm , the monolayer significantly depleted the amount of O_2 at the bottom of the model, resulting in significant gradients in z across the full computational volume. Spacing of 300 μm was very similar to 200 μm . Figure 4d–e shows the model in cases with O_2 supply from below as well as above, at a limited rate through Ibidi polymer slides in Figure 4d and at a more significant rate through a 200 μm thick layer of polydimethylsiloxane (PDMS) in Figure 4e. Critically comparing Figure 4b,e shows that, with O_2 supply arriving from multiple directions, the lateral and axial O_2 gradients are substantially reduced relative to the case with cells against glass (with O_2 arriving only from above), in both the intracellular and the extracellular spaces.

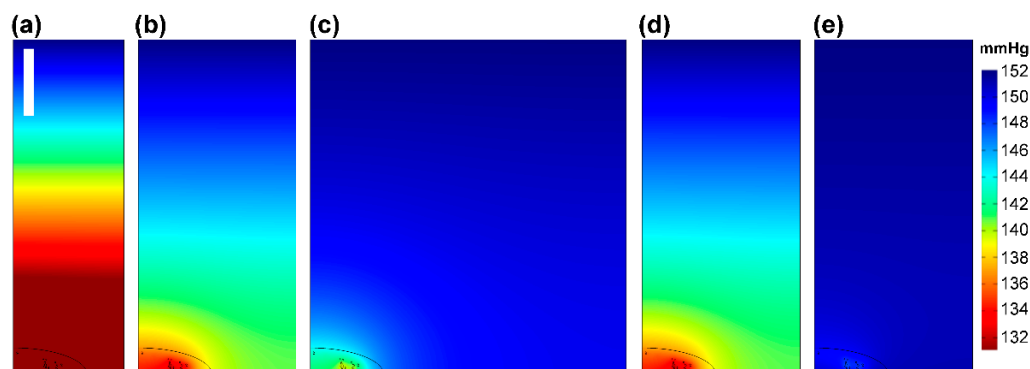


Figure 4. Confluence and substrate effects. The pO_2 (mmHg) slices of model with glass lower boundary at equilibrium with cell spacing of (a) 70 μm , (b) 100 μm , and (c) 200 μm , and with 100 μm spacing but lower boundary of (d) Ibidi polymer or (e) 200 μm PDMS, each over atmosphere. Planes through $y = x$ (i.e., diagonal to the square grid, in order to show longer dimension, shown by dotted line in Figure 3a). All panels are the same geometric scale; the scalebar in (a) is 30 μm . All panels are in the same color scale, as per bar at right.

3. Discussion

The model shows that, as seen *in vitro*, larger gradients are formed by cells against O_2 -impermeable substrates vs. those in suspension or on O_2 -permeable substrates. The computational results showing steep gradients in z and O_2 depletion, especially pronounced at lower applied O_2 levels, support the idea that cells growing on O_2 -impermeable surfaces are likely to deplete O_2 levels in their vicinity much more so than earlier models of cells in suspension predicted [3]. This is in line with the experimental results seen here, as well as published work on modeling O_2 delivery in tissue culture which has seen O_2 as a limiting factor in high-density monolayer culture [26].

The model and measurements both show $[O_2]$ in the mitochondrial compartment to be lower than that in the cytosol, with this difference decreasing in magnitude at the lowest ambient concentrations. Furthermore, the difference in pO_2 between mitochondrial and cytosolic compartments is relatively consistent between the experiment (1, 3, and 4 mmHg at applied $[O_2]$ of 5%, 10%, and 18.6%, respectively) and the model (up to 2.4 and 2.7 mmHg at applied $[O_2]$ of 5% and 20%), and relatively stable for the model at all but the lowest applied $[O_2]$ of 0.5% (0.4 mmHg based on the measurements and 0.4–0.8 mmHg based on the model). However, the intracellular O_2 concentrations measured with FLIM-FRET for higher values of imposed O_2 are substantially lower than those found for the same value of applied O_2 in the model. For example, intracellular O_2 found in the model for a 70 μm cell spacing and an applied $[O_2]$ of 10% is three times as high as that seen for experimental measurements with imposed pO_2 of 18.6%, although the intracellular O_2 found at 5% applied $[O_2]$ is consistent between measurement and model. To confirm whether the measured intracellular pO_2 levels are plausible, the expression of hypoxia-inducible factor (HIF)-1 α in HeLa cells was investigated at all applied O_2 %. On the basis of the results shown in Figure S2 (in Supplementary Materials), HIF-1 α was detected at all imposed O_2 %, even at 18.6%. The fact that we see essentially the same HIF-1 α expression level at 5% and hypoxia (when it should be less at 5%) means that the measured low intracellular pO_2 levels are indeed plausible [27]. These large differences between the absolute magnitude of $[O_2]$ in the experiments and model can likely be reconciled by considering how the imposed pO_2 measured with the OxyLite relates to the applied pO_2 fixed boundary used in the model calculations; the assumption that they are identical is almost certainly incorrect. This could arise from experimental factors, including uncertainty about the sampling volume of the OxyLite probe or nonuniformity of the cell layer, or from oversimplification in the model definition, particularly the omission of convective transport in the medium. The implications of this in interpreting the model are discussed in more detail in Section 3.3.

In addition, there are several factors we considered which might explain why the experimentally observed differences between pO_2 in mitochondrial and cytosolic compartments are slightly larger than those calculated in the model at higher applied $[O_2]$: (i) the observation of a gradient in pO_2 between the compartments partly arises from the presence of an *extracellular* O_2 gradient in the z direction; (ii) the potential localization of the FLIM-FRET probe through mitophagy within some unexpected compartment like lysosomes, where effects of the lysosomal refractive index and pH on the lifetime values obtained for Myo-mCherry may be confounding; (iii) other factors not considered in the model (e.g., active transport; significantly higher than expected barriers to O_2 diffusion in the membrane, etc.). Targeting of the indicator to compartments is not geometrically precise like the model. Since the periphery of the cell (further away from the center of mitochondrial mass) has higher pO_2 , another critical parameter in understanding the difference between mean 'mitochondrial' and 'cytosolic' $[O_2]$ is the mean distance beyond the extent of the central mitochondrial network (horizontally or vertically) that the 'cytosol' extends.

3.1. Effects of the Mitochondrial O_2 Consumption and Intracellular pO_2 Gradient in z

The scientific community generally accepts that cell culture is not a perfect model system. Three factors (O_2 above the medium, dissolved O_2 in the medium, and O_2 consumption by the cells) interact to create an $[O_2]$ gradient from the surface of the medium down to the surface of the cells [26]. This concentration gradient is the force that drives the flux of O_2 through the medium to the underlying cells. Modification of any of the above factors alters the gradient and, therefore, the rate of O_2 delivery to the cells [26].

The mitochondrial O_2 consumption of the cell monolayer at the bottom of the Petri dish is a major determinant of pericellular $[O_2]$ and, hence, the steepness of the O_2 gradient in the medium covering the cells [26]. To investigate this phenomenon, we used the OxyLite bare fiber probe to measure the imposed pO_2 (in mmHg) above the cell monolayer with and without respiring cells present. As shown in Figure 5a, mitochondrial O_2 consumption influenced the imposed pO_2 and, as a consequence, culture medium (without cells) and cells treated with rotenone/antimycin (non-consuming mitochondria) showed higher imposed pO_2 measurements than respiring cells [25]. We further explored the effect of ramping up mitochondrial O_2 consumption on the imposed pO_2 measurement by adding the uncoupler DNP, which causes cells to consume O_2 at a heightened rate, and we found a further reduction in the imposed pO_2 value measured with the OxyLite. Figure 5b shows the difference in measured pO_2 (ΔpO_2) as a function of cellular respiration and atmospheric $[O_2]$, obtained by subtracting the pO_2 values with cells present from those obtained for the medium (without cells). Please note that the OxyLite sensing volume is a porous hemisphere ~250 microns in diameter affixed to the fiber tip that measures the average medium pO_2 at levels everywhere from the dish surface to ~125 μm above, with average z distance of about 100 μm .

It is reported that the respiratory rate in cellular system is under enzymatic control over a wide range of pO_2 [28], and the question of whether or not the membrane is a barrier to O_2 transport can be relevant only at low concentrations. The question of the relative magnitudes of diffusion limitations in the surrounding medium and in the cell membrane is still unanswered. Herein, the gradient steepness between the medium and intracellular compartment was preliminarily evaluated with an external plasma membrane version of Myo-mCherry (pmMyo-mCherry). Lifetime imaging of pmMyo-mCherry was performed at various depths (z) to see the possible intracellular O_2 gradient in that direction. As shown in Figure 5c, the mean lifetime of pmMyo-mCherry was measured to be 1.18 ns in the basal plasma membrane, and there was a maximum of 6% lifetime increase when we moved 11 μm toward top of the cell surface; pO_2 changed from ~13.5 mmHg at basal plasma membrane to 47.7 mmHg at the top of the cell surface. Although further characterization of this probe is needed, it may be helpful in quantifying gradients across the cell and in assessing transport limitations that might arise from the membrane itself.

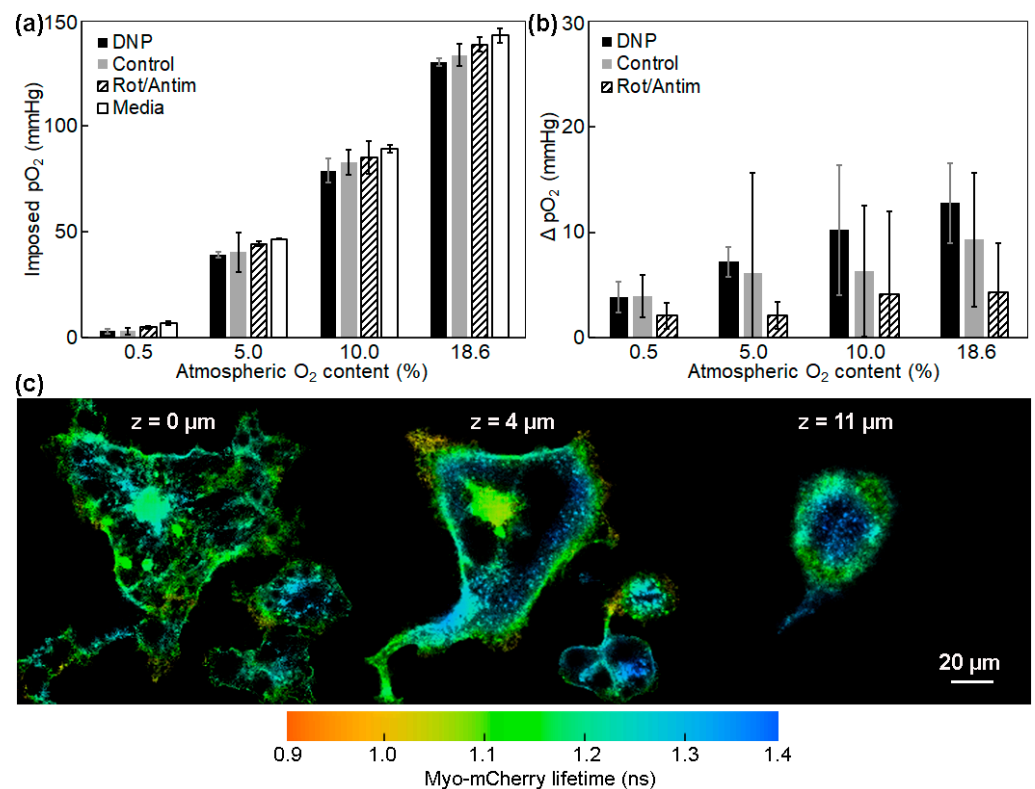


Figure 5. (a) The imposed pO₂ measured with OxyLite Pro in culture medium with or without respiring HeLa cells; the x axis represents the applied atmospheric O₂% in the stage incubator. (b) Change in O₂ concentration (ΔpO_2) measured with the OxyLite as a function of cellular respiration and applied pO₂, relative to values obtained for the medium (without cells). The error bars in (a,b) are the standard deviations. (c) Pseudocolor mapping of Myo-mCherry fluorescence lifetime in the plasma membrane of HeLa cells at different heights above the substrate. The cells were exposed to atmospheric [O₂] of 18.6%.

3.2. The Potential Effects of pH and Refractive Index on the Lifetime Values of Myo-mCherry

Due to many advances in methodology, the pH value and effective refractive index of cellular compartments have become widely known. In live HeLa cells, the pH values of the nucleus, cytoplasm, and mitochondria are reported to be 5.6, 7.1, and 7.9, respectively [29–31]. Lysosomes generate an acidic environment of pH 4.5–5.0 and accommodate hydrolytic enzymes to degrade engulfed biomolecules. Lysosomes also have the largest refractive index among the cellular organelles. In live HeLa cells suspended in culture medium, the refractive index measured by tomographic phase imaging was reported to be 1.355–1.365 RIU for the nucleus, 1.360–1.390 RIU for the cytoplasm, 1.400–1.420 RIU for the mitochondria, and 1.600 RIU for the lysosomes [32]. The inverse lifetime of green fluorescent protein (GFP) is a function of the refractive index squared of their environment [32]. Herein, we examined the possibility of either the degradation of Myo-mCherry in the lysosomes or lifetime change in a higher refractive index environment. Figure 6a compares the average lifetime values of Myo-mCherry in the cytosol of the HeLa cells with those in their lysosomes and mitochondria at different imposed O₂%. According to the Mann–Whitney U test, there was no statistically significant difference between the lifetime values obtained for lysosomes and cytosol ($p \geq 0.60$). Figure 6b shows the lifetime distribution of Myo-mCherry in the lysosomes of a typical HeLa cell at an atmospheric [O₂] of 5%. Lysosomal targeting did not shorten the lifetime values as expected vs. cytosol; in fact, a pronounced increase of the Myo-mCherry lifetime (~0.15 ns) is sometimes seen in some cells (region specified with a white square). However, this feature was only present in a small subpopulation of the HeLa cells.

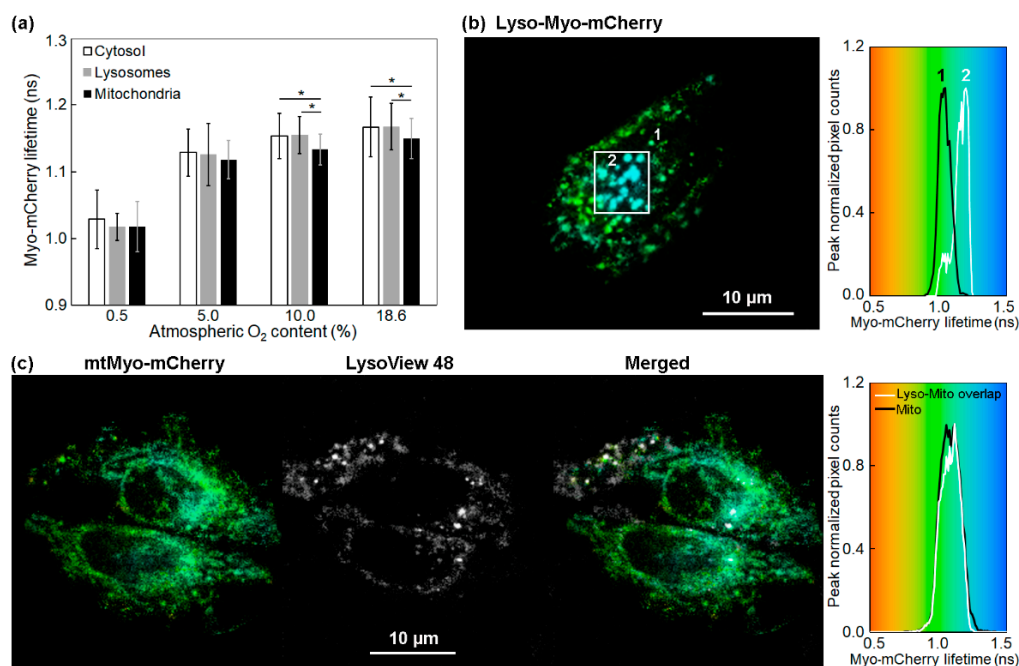


Figure 6. The changes of Myo-mCherry lifetime in HeLa cells using probes targeted to different subcellular compartments. **(a)** A comparison of the average fluorescence lifetime of Myo-mCherry in cytosol, lysosomes, and mitochondria; cells were exposed to external O₂% from 18.6% to 0.5%. The error bars are the standard deviations. * $p < 0.05$. **(b)** Pseudocolor mapping and distribution histogram of Lyso-Myo-mCherry fluorescence lifetime in a HeLa cell at 5% atmospheric [O₂]. **(c)** Pseudocolor mapping and distribution histogram of mtMyo-mCherry fluorescence lifetime in the mitochondria-lysosome contact environment.

Lastly, the effect of the higher lysosomal refractive index and lower pH on the lifetime values of Myo-mCherry in mitochondria–lysosome contact sites was also investigated. Mitochondria–lysosome contact sites were recently identified as inter-organelle membrane contacts involving the dynamic tethering of mitochondria with lysosomes. Importantly, mitochondria–lysosome contacts allow for the bidirectional regulation of both mitochondrial and lysosomal network dynamics, and they mediate their direct interaction in a pathway distinct from mitophagy or lysosomal degradation of mitochondrial-derived vesicles [33]. As shown in Figure 6c, the cells transfected with mtMyo-mCherry were labelled with LysoView 488 and changes in the lifetime of mtMyo-mCherry in the cross-correlated regions were inspected. Although, from 30% to 60% of the mitochondria overlapped with lysosomes, we did not see any significant difference between the lifetime in the cross-correlated regions and that in the whole cell.

3.3. Simplifications of O₂ Transport in Media

The computational model presented here is aimed at generally understanding intracellular O₂ concentrations and gradients, rather than predicting precise pericellular O₂ concentrations as a function of experimental conditions. Each calculation was performed with a fixed [O₂] at the upper boundary 150 μm above the cell substrate, and only considered diffusive transport in the medium. In the experimental setup, the [O₂] at this position depends heavily on convective and diffusive transport through the ~ 3 mm medium layer from the atmospheric supply to the O₂-consuming monolayer. Since consumption is only heterogeneous at the monolayer, the z-gradient caused by consumption is effectively uniform in x and y beyond a short distance from the lower boundary. Hence, the applied O₂ used in the model should not be directly compared to the atmospheric supply used experimentally, but rather understood as a simplification of a region where [O₂] is dictated by the experimental factors above. Values for these applied O₂ concentrations were

chosen to provide a variety of conditions, representative of the extracellular conditions measured experimentally.

As discussed above in Section 3.1, the OxyLite probe samples approximately a 250 μm hemisphere oriented downward, as close to the cell monolayer as possible without touching, expected to be approximately 125 μm above. At a first glance, it would seem that the OxyLite measurement of the imposed $p\text{O}_2$ should be reasonably well-matched to the upper boundary condition used in the computational model. However, there are a number of complicating factors and uncertainties.

First, since the OxyLite samples from an extended volume, the correspondence between the measured $p\text{O}_2$ values and the actual value at 150 μm above the substrate depends on the nature of the O_2 gradient in that region. It would not be surprising if the $[\text{O}_2]$ measured with the OxyLite was substantially higher than the immediate pericellular $[\text{O}_2]$ for experiments with active cellular respiration, particularly at higher levels of atmospheric O_2 . Due to the uncertainty in measurement depth for the OxyLite, it is likely that the model boundary $[\text{O}_2]$ that best matches the experimental conditions is lower than the extracellular concentration measured by the OxyLite. Second, the OxyLite measurements were taken over a culture area some distance from the imaging region, in order to avoid damaging the probe with the two-photon pulsed laser. It is possible that the density of the monolayer (and hence its O_2 consumption) could differ between these two regions. Third, cells in the experiments were significantly more confluent (phase contrast images of the cell confluency in Figure S3 in Supplementary Materials) than the modeled cells. While not expected to significantly affect the intracellular gradients seen, this *would* have a significant impact on the gradient in z and on the pericellular $[\text{O}_2]$. Fourth, there is convective transport in the medium, and it is possible that this is the dominant transport mechanism at least through the upper parts of the 3 mm medium layer. The relative size of contributions from convection and diffusion in this experimental setup over the much smaller distances considered in the computational model is an open question, but it is likely that convection affects the shape of the z -gradient in the region sampled by the OxyLite probe.

3.4. Uncertainty in Intracellular O_2 Transport Mechanisms

Diffusion has historically been considered the primary driver of molecular transport within the cell [34]. However, intracellular convection has been observed in highly motile cells [35]. Since our model and experiments consider adherent cells over short timescales, motility is unlikely to play a role in generating intracellular convective currents. There is also some controversial evidence that intracellular thermal gradients may be large enough to create convective currents in motionless cells [36]. We would expect such currents to reduce the magnitude of intracellular O_2 gradients. On the other hand, there is some contention over the effective rate of O_2 diffusion in the densely packed intracellular environment. While our calculations here used ‘consensus’ values for this diffusion constant, if it were to be significantly lower, the model calculations would yield larger intracellular gradients. For example, if cytosol were significantly less permeable to O_2 than extracellular/interstitial paths, that heterogeneity would make bulk measurement of packed cell diffusion rates more a measure of interstices than cytosol. O_2 diffusion on the nanoscale may, thus, differ from that seen across millimeters. The model here should be considered a basic framework for understanding intracellular O_2 gradients that can arise in the diffusion-dominated regime. In the event that future work develops a more detailed understanding of intracellular O_2 transport parameters, the model will need to be amended.

Due to the computational demands of complex geometries, this model also only considers one-quarter of a cell in a uniform square grid. Acknowledging that cell seeding cannot be perfectly uniform, the average conditions experienced by cells may differ in clusters. It is likely that local conditions vary widely from this average case, either within clusters or more complicated geometries. The data shown in Figure 4 show that, well below confluence, sparsely spaced cells do not create significantly different gradients, but closer spacings or heterogeneous cells are likely to produce different gradients.

4. Materials and Methods

4.1. FLIM-Based Oxygen Probes

Plasmids containing the untargeted myoglobin-mCherry (cytosolic Myo-mCherry), myoglobin-mCherry fused to the TFAM mitochondrial targeting sequence (MTS) (mtMyo-mCherry), myoglobin-mCherry targeted to the lysosomes (Lyso-Myo-mCherry), and myoglobin-mCherry fused to the RP2 plasma membrane targeting sequence (N-PM-Gly3-Myo-mCherry) were made for the intracellular O₂ measurements. The untagged form of mCherry (alone) with no myoglobin or its fused form to mitochondria MTS (mt-mCherry) served as O₂ insensitive controls for FLIM measurements [24]. The localization of mtMyo-mCherry and Lyso-Myo-mCherry was confirmed by mitoTracker Green and LysoView 488, respectively.

4.2. Cell Transfection with O₂ Probes

HeLa cells were plated in eight-well chamber microscope slides (Ibidi GmbH, Martinsried, Germany) at a density of 2×10^4 cells/cm² in Modified Eagle Medium (DMEM, Gibco, Grand Island, NY, USA) with 10% fetal bovine serum (FBS, Mediatech Inc., Manassas, VA, USA) and 1% penicillin–streptomycin (Mediatech Inc., Manassas, VA, USA). Prior to transfection, the cells were placed into DMEM containing 20% FBS and antibiotics. The transfection medium was prepared by diluting 10 µg of the appropriate plasmid DNA and 20 µL of P3000 reagent (Invitrogen, Carlsbad, CA, USA) in 500 µL of Opti-MEM[®] medium (Gibco, Thermo Fisher Scientific Inc., Grand Island, NY, USA). This was combined with a solution of 10 µL of Lipofectamine[®] 3000 transfection reagent (Invitrogen, Carlsbad, CA, USA) in 500 µL of Opti-MEM[®] medium and vortexed. The transfection medium was allowed to activate for 15 min before it was added to cells with a final plasmid amount of 2 µg of mtMyo-mCherry and Lyso-Myo-mCherry or 0.1 µg of Myo-mCherry and PM-Gly3-Myo-mCherry. The cells were incubated in this transfection medium for 24 h at 37 °C and 5% CO₂, after which the cells were washed and covered with fresh cell medium containing 20% FBS as before. Cells were imaged 48 h after transfection.

4.3. Mitochondrial Modulator Treatment

Cells were treated with 2 µM rotenone and 2 µM antimycin A (AA) inhibitors or 50 µM 2,4-dinitrophenol (DNP) uncoupler for modulating the mitochondrial O₂ consumption.

4.4. FLIM Setup

An Olympus IX81 confocal laser scanning microscope (Melville, NY, USA) equipped with a tunable Mai Tai BB DeepSee femtosecond laser (Spectra-Physics, Santa Clara, CA, USA) with wavelengths set to 780 nm was used for two-photon FLIM. The laser light was passed through a 690 nm dichroic mirror and directed to an Olympus UPLANSAPO 60×, 1.2 NA water immersion objective. A 675 nm short pass and a 647/57 nm bandpass filter (both from Semrock BrightLine[®], Rochester, NY, USA) were used to reduce scattered light and to filter the mCherry signal, respectively. The fluorescence was detected using a PMC100 cooled detector (Becker & Hickl GmbH, Berlin, Germany), and the electrical pulse output from the detector was directed into an SPC-150N photon counting card (Becker & Hickl). For time-correlated single photon counting (TCSPC), the signals were synchronized with the pulses from the laser. Then, synchronization with the pixel, line, and frame clock from the scanning unit of the microscope was used for image construction in TCSPC mode. The cells were excited with a laser power ≤18 mW and imaged for 40–80 s to accumulate an adequate number of photons per pixel and to avoid photobleaching and photocytotoxicity. Image size was set to 256 × 256 (pixels)², and TCSPC histograms were collected with 256 channels.

A miniature cell incubator connected to a gas mixing system (CO₂–O₂–MI, Bioscience Tools, San Diego, CA, USA) was mounted onto the microscope stage to provide a suitable cellular environment during imaging. The incubator kept the temperature at 37 °C, and the gas mixing system delivered mixtures of N₂, O₂, and CO₂ inside the chamber according to

the inputs set by the user. FLIM recordings were performed at stable %O₂ (v/v) of 18.6%, 10%, 5%, and 0.5% in the microscope incubator, where 0.5% is the lowest %O₂ attainable by our system. Typically, the cell culture (in culture dishes with a ~3 mm layer of medium above cells, without lids), when monitored by a 250 μm diameter bare-fiber O₂ sensor (NX-BF/O/E, Optronix Ltd., Oxford, UK) connected to an OxyLite 1 Channel monitor (Optronix Ltd., Oxford, UK), reaches a stable pO₂ within 1 h. The medium-imposed external pO₂ (in mmHg) was measured at the bottom of the petri dish with or without live cells present. FLIM and OxyLite measurements were performed in the same experimental runs (the same cells and petri dishes).

4.5. Fluorescence Microscopy

For 3D imaging of the mitochondria distribution and investigation of mitochondria/lysosomes contact sites, the cells were incubated in 100 nM MitoTracker Green FM 100 (Invitrogen) or transfected with mtMyoglobin-mCherry and labeled with 10 μg/mL LysoView™ 488 (Biotium, Fremont, CA, USA) at 37 °C for 30 min, respectively. Cells were washed three times with prewarmed cell culture medium. The 3D images of the mitochondria were acquired using a Zeiss LSM 780 confocal microscope (Carl Zeiss, Germany) equipped with a 63× oil immersion objective. MitoTracker Green was excited by an Argon 488 nm laser, and the fluorescence was directed toward a Photomultiplier Tube (PMT). Then, the green signals were spectrally filtered by an adjustable bandpass filter in photon-counting mode set to 499–534 nm. The cross-correlations between the signals of mtMyoglobin-mCherry/LysoView 488 and lifetime imaging of mtMyo-mCherry were performed using the Olympus IX81 confocal laser scanning microscope with wavelengths set to 780 nm for the excitation of mCherry and 880 nm for the excitation of LysoView. The emissions were collected using a bandpass filter 520/60 nm for LysoView 488 and a bandpass filter 647/57 nm for mCherry.

4.6. FLIM Analysis and Intracellular Mapping of pO₂

FLIM images were processed as previously described [23]. Briefly, the fluorescence lifetime decays of Myo-mCherry in the whole cell, mitochondria, lysosomes, or plasma membrane were obtained by a double-exponential decay model in SPCImage (Becker & Hickl) at optimized goodness of fit (χ^2). The mean lifetime was obtained for each single image (via amplitude weighting for each pixel) and averaged across multiple cells ($n > 30$). Then, the resulting lifetime values ($\tau(pO_2)$) were plotted against the medium-imposed external pO₂ and a hyperbolic curve was fit to the data using MATLAB R2020b (The MathWorks Inc., Natick, MA, USA):

$$\tau(pO_2) = (\tau_{max} - 0.96) \frac{pO_2}{K + pO_2} + 0.96, \quad (1)$$

where τ_{max} is the longest average lifetime for Myo-mCherry at normoxia (O₂ = 18.6%), and K is a fitting parameter related to the affinity of myoglobin for O₂. The $\tau(pO_2)$ values for non-respiring cells (those treated with rotenone/antimycin) were used as a reference for the lifetime of the probe at the environmental level of pO₂ present in solution. Rearranging Equation (1), fixing the K and τ_{max} to the values obtained from the reference curve, the effective pO₂ at each lifetime value was back-calculated for the respiring cells. Then, pseudocolor mappings of pO₂ in the cytosolic and mitochondrial environments were obtained using MATLAB R2020b (The MathWorks Inc.) equipped with the Image Processing Toolbox. More detailed description can be found in our earlier work [23].

Please note that the hyperbolic binding formula above yields widely varying pO₂ values where the slope is small, i.e., above 50 mmHg, where the myoglobin is fully saturated with O₂. Thus, we truncate color coding images at 50 mmHg and above.

4.7. Statistical Analysis

For each condition, FLIM was recorded in at least 30 cells. Kruskal–Wallis or Mann–Whitney U tests were used to evaluate whether the values in the independent groups are significantly different from each other. Analyses were carried out using SPSS 14.0 (a subsidiary of IBM, Chicago, IL, USA) software and statistical significance was defined at $p < 0.05$ (95% confidence level).

4.8. COMSOL Simulation of Intracellular pO_2 Gradients

We modeled O_2 gradients using finite-element analyses performed with the COMSOL Multiphysics Chemical Reaction Engineering Module. One-quarter of a cell's mitochondrial network was modeled in a column of medium as shown in Figure 2. Symmetric boundary conditions (as described below) were applied on the four sides of the column such that results generalized to a case of a uniform square monolayer of symmetric cells. Oxygen concentration was fixed at an applied level at the top of the medium column to represent exchange with the larger volume of medium where convection was presumably the dominant mechanism of gas exchange. According to the density of macromolecules and other solutes in the cytoplasm, a lower O_2 diffusion rate was used for it than in the bulk medium, in line with experimental measurements and that used in other models [37–42].

A realistic model of 3D mitochondrial structure was generated from imaging of C2C12 mouse myoblasts cells treated with MitoTracker Green FM (Invitrogen) as described above, and imaged with a pixel size of $108 \times 108 \times 100$ nm (xyz) (Figure S1). While O_2 consumption rate can vary widely in different conditions, similarly measured C2C12 and HeLa cells have shown per-cell consumption values within 5% of one another [43]. Image stacks were deconvolved using Huygens SVI on the basis of five point-spread functions measured using $0.1 \mu\text{m}$ microspheres, fluorescent blue/green/orange/dark red (TetraSpeckTM, Invitrogen). A representative cell was chosen for developing the 3D model. Initial postprocessing to binary images was performed in ImageJ following established protocol [44]. Since deconvolved images still showed stretching in z due to the acquisition method, binaries were then converted into skeletons using the `bwskel` function in the MATLAB R2020b Image Processing Toolbox (The MathWorks Inc., Natick, MA, USA). Due to the computational demands of larger models, one-quarter of this skeletonized model was used.

Slicer 3D was used to convert binary skeletons into STL meshes [45]. Volume geometry was adjusted to the correct spacing of the microscope raster. The volume was then oversampled by a factor of approximately two in each dimension to improve the handling of narrow and curved regions. Anisotropy was enforced during oversampling for a final pixel size of 50 nm in each dimension. An Otsu threshold was used to determine initial segmentation of mitochondrial volumes. The subsequent steps were performed according to what was observed to produce a model that balanced the geometric complexity of the volume with the constraints of simplicity needed for simulation. The following morphological operations were performed: grown on margin by four pixels, sliced into nine pieces with yz planes to reduce connectivity (without which extensively connected pieces were too complex to simulate), opened by nine pixels, median-filtered by seven pixels, opened by seven pixels, removed islands smaller than 2500 pixels, and closed by three pixels.

The resulting STL mesh was loaded into COMSOL with automatically determined repair tolerance and boundary partitioning and then imported into the model geometry with a relative simplification tolerance of 0.01 and a defect removal factor of 1.02. To ensure smooth modeling of high convoluted structures, models were meshed with a minimum element size of 1 nm.

The finalized geometry was placed close to the lower boundary of the model described above. Similarly, radii of the eighth-ellipsoid section representing the boundary between cytoplasm and medium were chosen on the basis of the smallest size that fit the full mitochondrial network without generating sections too thin for successful meshing: $30 \times 30 \times 12 \mu\text{m}$ (xyz). Unit model cell sizes of 35, 50, 100, and $150 \mu\text{m}$ correspond to

center-to-center cell spacings of 70, 100, 200, and 300 μm or to cell seeding densities of 2.4×10^4 , 1×10^4 , 2.5×10^3 , and 1.1×10^3 cells/ cm^2 , respectively (in a uniform square grid). Gradients observed at spacings greater than 200 μm were not largely different than those seen at 200 μm spacing; thus, data from those models are not presented here, and larger spacings than 300 μm were not simulated.

Intracellular O_2 transport was assumed to be governed by Fickian diffusion within all domains, with the addition of a term for consumption giving the following overall equation:

$$\frac{\partial c}{\partial t} = D\nabla^2 c + R, \quad (2)$$

where c represents the concentration, D is the diffusivity, and R is the volume consumption rate (all for O_2) [46]. R was assumed to be nonzero only in mitochondria, and the diffusion coefficient and solubility parameters of the mitochondria were assumed to be equal to that of the cytosol [47]. Exact values of O_2 solubility and diffusion in complex, solute-dense environments such as growth medium and even more so intracellular regions are contentious topics with limited experimental data [26]. These two sets of parameters were treated as the minimum, average, or maximum reliable literature values for the slow, standard, and fast diffusion conditions.

Symmetric boundaries were used to reduce the computational complexity of the model. The boundary condition applied to O_2 concentrations at such boundaries was

$$0 = -\mathbf{n} \cdot (-D\nabla^2 c). \quad (3)$$

The O_2 consumption rate in cells is highly dependent on coupling between metabolic pathways and cellular state. However, the overall pathway O_2 consumption rate under steady-state conditions can be modeled as a hyperbolic, Michaelis–Menten style function of local O_2 concentration:

$$R = V_{\max} \frac{c}{K_m + c} \quad (4)$$

where V_{\max} represents the maximum O_2 consumption rate, and K_m represents the apparent concentration at which the rate is half-maximal, which depend on the metabolic state and internal structure of the particular mitochondrion [48,49]. We modeled consumption of the form in Equation (4) with constant V_{\max} and K_m within a single mitochondrion as a volume reaction.

To set an upper bound on possible O_2 consumption within a single mitochondrion, metabolic estimates based on respirometry of honeybee (*Apis mellifera*) flight muscles were used, as they are thought to represent maximal respiration rates [50–52]. Notably, these values exceed the greatest values estimated or measured for mammalian mitochondria by an order of magnitude. Simulations were also run with upper limit measured values from high-resolution respirometry of isolated mitochondria/muscle tissue and full body respiratory measurements, of which the latter exceed the former by a factor of three [53,54]. Simulations were performed with these extreme values for maximal consumption rate in order to determine the steepest gradients plausible. A factor in overall consumption rates in the cell is the total volume of mitochondria. While our imaging substantially captures the shape of mitochondrial networks in the cell, there is significant room for error and interpretation in determining the volume of those networks, and this may have led to our results under or overestimating total consumption of the cell.

Although diffusion across intracellular membranes is not thought to be a significant barrier to O_2 diffusion compared to through aqueous environments [11], inward O_2 flux across boundaries was modeled as

$$P \left(c_o - \frac{S_o}{S_i} c_i \right) = -\mathbf{n} \cdot (-P\nabla c_i), \quad (5)$$

where c_o and c_i represent the concentrations in the external and internal domains, respectively, S_o and S_i represent the solubilities in the external and internal domains, respectively, n represents the normal unit vector to the boundary, and P represents the boundary's permeability to O_2 [55]. The polymer bottom of the slide was treated as a thin boundary with mass transfer coefficient k between the cytosol and ambient air (assumed to be convectively maintained at constant pO_2).

The incubator's controlled atmospheric inflow was assumed to provide convective mixing and bulk flow to assure a relatively constant O_2 tension. Hence, the O_2 concentration at the upper simulated limit of the medium was constrained to the value predicted by Henry's law in the applied atmosphere:

$$c = SpO_2, \quad (6)$$

where pO_2 is the partial pressure of O_2 in the incubator, and S is the solubility of O_2 in the medium. This applied O_2 value may not correspond one-to-one with experimentally applied O_2 values due to differences in medium thickness between experiments. Furthermore, assuming no convection and that O_2 consumption is uniform across the surface of the slide, the majority of the O_2 gradient is effectively 1D through the medium column until just above the consumption; hence, changing medium depth beyond a few factors of cell thickness is indistinguishable from changing the applied pO_2 .

In order to better understand how consumption differs in an environment with O_2 supply from multiple directions instead of just from above (as is experienced by cells in suspension, for example), an alternative model with a layer of O_2 -permeable polydimethylsiloxane as the lower boundary was developed.

Lastly, since O_2 -permeable Ibidi culture slides were used for imaging, the lower boundary of the cell was considered an inflow of O_2 per the manufacturer's measured mass-transfer coefficient assuming that convection controlled the exterior [O_2] to be the ambient concentration throughout. The values used in the model are shown in Table 3.

Table 3. Parameters used for simulation.

Description	Symbol [Units]	Element	Value	References
O_2 diffusivity 'consensus'	D [cm ² /s]	Medium,	1.9×10^{-5}	[16,26,56–58]
		intracellular	0.9×10^{-5}	[37–42]
		PDMS	5×10^{-5}	[59]
O_2 solubility	S [mol/cm ³ /mmHg]	Medium, intracellular	1.29×10^{-3}	[16,38,60,61]
		PDMS	1.06×10^{-2}	[59]
O_2 permeability	P [cm/s]	Membrane	42	[11]
		PDMS	8	[62]
Slide mass transfer coefficient	k [mol/cm ² /s/bar O_2]	Slide	7.19×10^{-12}	Ibidi manufacturer
Maximum O_2 consumption rate	V_{\max} [mol/m ³ /s]	Mitochondria	10	[37,38,43,50,63]
[O_2] at half-maximal rate	K_m [mol/m ³]	Mitochondria	1×10^{-4}	[26,58,64,65]

5. Conclusions

We investigated intracellular pO_2 in HeLa cells with computational modeling and fluorescence lifetime imaging. The computational data quantitatively agree with experimental results on O_2 heterogeneity in the intracellular environment and provide insight into further predictions and impact of mitochondrial O_2 consumption. Dimensional arguments and the measurement of diffusion in bulk tissue have long predicted the absence of significant intracellular O_2 gradients; hence, we viewed our now-frequent observations of the same

with a jaundiced eye. To date, however, we were unable to find fault with the observations themselves, as we systematically examined a variety of alternative explanations for the fluorescence lifetime changes seen, identifying no artifact yet. We observed, however, that the cell culture environment presents opportunities for low-dimension behavior; the cell that is ‘living with its back against an O₂-impermeable wall’, especially at confluence, is clearly different from one in tissue.

Supplementary Materials: The supporting information can be downloaded at <https://www.mdpi.com/article/10.3390/ijms232012597/s1>.

Author Contributions: COMSOL simulations, writing, and editing, A.J.H.S.; FLIM and fluorescence confocal imaging, data analyses, and writing—original draft, review, and editing, R.P.; FLIM and plate-reader measurements, K.A.L.; cell culture and transfection, as well as the preparation of the plasma membrane targeting probe, A.B.; lysosome-targeting probe, J.K.; HIF-1 α immunoblotting, S.-J.P.; resources, supervision, methodology, and funding acquisition, J.H.C., N.Y.M. and J.R.K. All authors have read and agreed to the published version of the manuscript.

Funding: This work was supported by the Intramural Research Program of the National Heart, Lung, and Blood Institute (NHLBI), the National Institute of Biomedical Imaging and Bioengineering (NIBIB) at the National Institutes of Health (NIH).

Institutional Review Board Statement: Not applicable.

Informed Consent Statement: Not applicable.

Data Availability Statement: Data are available on request due to privacy or other restrictions.

Acknowledgments: We thank the Light Microscopy Core at NHLBI (especially Christian Combs) for helpful discussions and the use of their confocal microscopes for fluorescence intensity measurements. We thank Shutong Yang of NHLBI and George Patterson of NIBIB for assistance in designing and preparing plasma membrane targeted Myo-mCherry and different plasmids for our various chimeric sensors. We thank Han Tran of NIBIB for assistance with generation of figures using COMSOL.

Conflicts of Interest: The authors declare no conflict of interest.

References

1. Wilson, D.F.; Rumsey, W.L.; Green, T.J.; Vanderkooi, J.M. The oxygen dependence of mitochondrial oxidative phosphorylation measured by a new optical method for measuring oxygen concentration. *J. Biol. Chem.* **1988**, *263*, 2712–2718. [[CrossRef](#)]
2. Wilson, D.F. Oxidative phosphorylation: Regulation and role in cellular and tissue metabolism. *J. Physiol.* **2017**, *595*, 7023–7038. [[CrossRef](#)] [[PubMed](#)]
3. Clark, A., Jr.; Clark, P.A. Local oxygen gradients near isolated mitochondria. *Biophys. J.* **1985**, *48*, 931–938. [[CrossRef](#)]
4. Grinberg, O.Y.; James, P.E.; Swartz, H.M. Are there Significant Gradients of pO₂ in Cells. In *Oxygen Transport to Tissue XX*; Hudetz, A.G., Bruley, D.F., Eds.; Springer: Boston, MA, USA, 1998; pp. 415–423. ISBN 978-1-4615-4863-8. [[CrossRef](#)]
5. Glockner, J.F.; Swartz, H.M.; Pals, M.A. Oxygen gradients in CHO cells: Measurement and characterization by electron spin resonance. *J. Cell. Physiol.* **1989**, *140*, 505–511. [[CrossRef](#)]
6. Takahashi, E.; Sato, K.; Endoh, H.; Xu, Z.L.; Doi, K. Direct observation of radial intracellular pO₂ gradients in a single cardiomyocyte of the rat. *Am. J. Physiol.* **1998**, *275*, H225–H233. [[CrossRef](#)]
7. Katz, I.R.; Wittenberg, J.B.; Wittenberg, B.A. Monoamine oxidase, an intracellular probe of oxygen pressure in isolated cardiac myocytes. *J. Biol. Chem.* **1984**, *259*, 7504–7509. [[CrossRef](#)]
8. Jones, D.P. Intracellular diffusion gradients of O₂ and ATP. *Am. J. Physiol.* **1986**, *250*, C663–C675. [[CrossRef](#)]
9. Kennedy, F.G.; Jones, D.P. Oxygen dependence of mitochondrial function in isolated rat cardiac myocytes. *Am. J. Physiol.* **1986**, *250*, C374–C383. [[CrossRef](#)]
10. Robiolio, M.; Rumsey, W.L.; Wilson, D.F. Oxygen diffusion and mitochondrial respiration in neuroblastoma cells. *Am. J. Physiol.* **1989**, *256*, C1207–C1213. [[CrossRef](#)]
11. Subczynski, W.K.; Hopwood, L.E.; Hyde, J.S. Is the mammalian cell plasma membrane a barrier to oxygen transport? *J. Gen. Physiol.* **1992**, *100*, 69–87. [[CrossRef](#)]
12. Clark, A.; Clark, P.A.; Connett, R.J.; Gayeski, T.E.; Honig, C.R. How large is the drop in pO₂ between cytosol and mitochondrion? *Am. J. Physiol.* **1987**, *252*, C583–C587. [[CrossRef](#)] [[PubMed](#)]
13. Hermán, P.; Trübel, H.K.; Hyder, F. A Multiparametric Assessment of Oxygen Efflux from the Brain. *J. Cereb. Blood Flow Metab.* **2006**, *26*, 79–91. [[CrossRef](#)] [[PubMed](#)]

14. Hirai, D.M.; Colburn, T.D.; Craig, J.C.; Hotta, K.; Kano, Y.; Musch, T.I.; Poole, D.C. Skeletal muscle interstitial O₂ pressures: Bridging the gap between the capillary and myocyte. *Microcirculation* **2019**, *26*, e12497. [[CrossRef](#)] [[PubMed](#)]
15. Skattebo, Ø.; Calbet, J.A.L.; Rud, B.; Capelli, C.; Hallén, J. Contribution of oxygen extraction fraction to maximal oxygen uptake in healthy young men. *Acta Physiol. Oxf. Engl.* **2020**, *230*, e13486. [[CrossRef](#)]
16. Leshner-Pérez, S.C.; Kim, G.-A.; Kuo, C.-H.; Leung, B.M.; Mong, S.; Kojima, T.; Moraes, C.; Thouless, M.D.; Luker, G.D.; Takayama, S. Dispersible oxygen microsensors map oxygen gradients in three-dimensional cell cultures. *Biomater. Sci.* **2017**, *5*, 2106–2113. [[CrossRef](#)]
17. Kutala, V.K.; Parinandi, N.L.; Pandian, R.P.; Kuppusamy, P. Simultaneous measurement of oxygenation in intracellular and extracellular compartments of lung microvascular endothelial cells. *Antioxid. Redox Signal.* **2004**, *6*, 597–603. [[CrossRef](#)]
18. Mizukami, K.; Katano, A.; Shiozaki, S.; Yoshihara, T.; Goda, N.; Tobita, S. In vivo O₂ imaging in hepatic tissues by phosphorescence lifetime imaging microscopy using Ir(III) complexes as intracellular probes. *Sci. Rep.* **2020**, *10*, 21053. [[CrossRef](#)]
19. Kurokawa, H.; Ito, H.; Inoue, M.; Tabata, K.; Sato, Y.; Yamagata, K.; Kizaka-Kondoh, S.; Kadonosono, T.; Yano, S.; Inoue, M.; et al. High resolution imaging of intracellular oxygen concentration by phosphorescence lifetime. *Sci. Rep.* **2015**, *5*, 10657. [[CrossRef](#)]
20. James, P.E.; Grinberg, O.Y.; Michaels, G.; Swartz, H.M. Intraphagosomal oxygen in stimulated macrophages. *J. Cell. Physiol.* **1995**, *163*, 241–247. [[CrossRef](#)]
21. Rajagopal, V.; Bass, G.; Ghosh, S.; Hunt, H.; Walker, C.; Hanssen, E.; Crampin, E.; Soeller, C. Creating a Structurally Realistic Finite Element Geometric Model of a Cardiomyocyte to Study the Role of Cellular Architecture in Cardiomyocyte Systems Biology. *J. Vis. Exp.* **2018**, *134*, 56817. [[CrossRef](#)]
22. Ghosh, S.; Tran, K.; Delbridge, L.M.D.; Hickey, A.J.R.; Hanssen, E.; Crampin, E.J.; Rajagopal, V. Insights on the impact of mitochondrial organisation on bioenergetics in high-resolution computational models of cardiac cell architecture. *PLoS Comput. Biol.* **2018**, *14*, e1006640. [[CrossRef](#)]
23. Penjweini, R.; Roarke, B.; Alspaugh, G.; Gevorgyan, A.; Andreoni, A.; Pasut, A.; Sackett, D.L.; Knutson, J.R. Single cell-based fluorescence lifetime imaging of intracellular oxygenation and metabolism. *Redox Biol.* **2020**, *34*, 101549. [[CrossRef](#)] [[PubMed](#)]
24. Penjweini, R.; Andreoni, A.; Rosales, T.; Kim, J.; Brenner, M.D.; Sackett, D.L.; Chung, J.H.; Knutson, J.R. Intracellular oxygen mapping using a myoglobin-mCherry probe with fluorescence lifetime imaging. *J. Biomed. Opt.* **2018**, *23*, 107001. [[CrossRef](#)]
25. Keeley, T.P.; Mann, G.E. Defining Physiological Normoxia for Improved Translation of Cell Physiology to Animal Models and Humans. *Physiol. Rev.* **2019**, *99*, 161–234. [[CrossRef](#)] [[PubMed](#)]
26. Place, T.L.; Domann, F.E.; Case, A.J. Limitations of oxygen delivery to cells in culture: An underappreciated problem in basic and translational research. *Free Radic. Biol. Med.* **2017**, *113*, 311–322. [[CrossRef](#)]
27. Jiang, B.H.; Semenza, G.L.; Bauer, C.; Marti, H.H. Hypoxia-inducible factor 1 levels vary exponentially over a physiologically relevant range of O₂ tension. *Am. J. Physiol.* **1996**, *271*, C1172–C1180. [[CrossRef](#)]
28. Dexter, S.T. Respiratory Rate and Enzyme Activity as Related to the Hardened Condition of Plants. *Plant Physiol.* **1934**, *9*, 831–837. [[CrossRef](#)]
29. Hou, H.; Zhao, Y.; Li, C.; Wang, M.; Xu, X.; Jin, Y. Single-cell pH imaging and detection for pH profiling and label-free rapid identification of cancer-cells. *Sci. Rep.* **2017**, *7*, 1759. [[CrossRef](#)]
30. Llopis, J.; McCaffery, J.M.; Miyawaki, A.; Farquhar, M.G.; Tsien, R.Y. Measurement of cytosolic, mitochondrial, and Golgi pH in single living cells with green fluorescent proteins. *Proc. Natl. Acad. Sci. USA* **1998**, *95*, 6803–6808. [[CrossRef](#)]
31. Ponsford, A.H.; Ryan, T.A.; Raimondi, A.; Cocucci, E.; Wycislo, S.A.; Frohlich, F.; Swan, L.E.; Stagi, M. Live imaging of intralysosome pH in cell lines and primary neuronal culture using a novel genetically encoded biosensor. *Autophagy* **2021**, *17*, 1500–1518. [[CrossRef](#)]
32. Liu, P.Y.; Chin, L.K.; Ser, W.; Chen, H.F.; Hsieh, C.M.; Lee, C.H.; Sung, K.B.; Ayi, T.C.; Yap, P.H.; Liedberg, B.; et al. Cell refractive index for cell biology and disease diagnosis: Past, present and future. *Lab Chip* **2016**, *16*, 634–644. [[CrossRef](#)] [[PubMed](#)]
33. Kim, S.; Wong, Y.C.; Gao, F.; Krainc, D. Dysregulation of mitochondria-lysosome contacts by GBA1 dysfunction in dopaminergic neuronal models of Parkinson's disease. *Nat. Commun.* **2021**, *12*, 1807. [[CrossRef](#)] [[PubMed](#)]
34. Trovato, F.; Tozzini, V. Diffusion within the Cytoplasm: A Mesoscale Model of Interacting Macromolecules. *Biophys. J.* **2014**, *107*, 2579–2591. [[CrossRef](#)]
35. Keren, K.; Yam, P.T.; Kinkhabwala, A.; Mogilner, A.; Theriot, J.A. Intracellular fluid flow in rapidly moving cells. *Nat. Cell Biol.* **2009**, *11*, 1219–1224. [[CrossRef](#)] [[PubMed](#)]
36. Howard, R.; Scheiner, A.; Cunningham, J.; Gatenby, R. Cytoplasmic convection currents and intracellular temperature gradients. *PLoS Comput. Biol.* **2019**, *15*, e1007372. [[CrossRef](#)] [[PubMed](#)]
37. Chow, D.C.; Wenning, L.A.; Miller, W.M.; Papoutsakis, E.T. Modeling pO₂ distributions in the bone marrow hematopoietic compartment. I. Krogh's model. *Biophys. J.* **2001**, *81*, 675–684. [[CrossRef](#)]
38. Chow, D.C.; Wenning, L.A.; Miller, W.M.; Papoutsakis, E.T. Modeling pO₂ distributions in the bone marrow hematopoietic compartment. II. Modified Kroghian models. *Biophys. J.* **2001**, *81*, 685–696. [[CrossRef](#)]
39. Fischkoff, S.; Vanderkooi, J.M. Oxygen diffusion in biological and artificial membranes determined by the fluorochrome pyrene. *J. Gen. Physiol.* **1975**, *65*, 663–676. [[CrossRef](#)]
40. Vadapalli, A.; Pittman, R.N.; Popel, A.S. Estimating oxygen transport resistance of the microvascular wall. *Am. J. Physiol.-Heart Circ. Physiol.* **2000**, *279*, H657–H671. [[CrossRef](#)]

41. Carrier, R.L.; Rupnick, M.; Langer, R.; Schoen, F.J.; Freed, L.E.; Vunjak-Novakovic, G. Perfusion Improves Tissue Architecture of Engineered Cardiac Muscle. *Tissue Eng.* **2002**, *8*, 175–188. [[CrossRef](#)]
42. Goldstick, T.K.; Ciuryla, V.T.; Zuckerman, L. Diffusion of oxygen in plasma and blood. *Adv. Exp. Med. Biol.* **1976**, *75*, 183–190. [[PubMed](#)]
43. Wagner, B.A.; Venkataraman, S.; Buettner, G.R. The rate of oxygen utilization by cells. *Free Radic. Biol. Med.* **2011**, *51*, 700–712. [[CrossRef](#)] [[PubMed](#)]
44. Chaudhry, A.; Shi, R.; Luciani, D.S. A pipeline for multidimensional confocal analysis of mitochondrial morphology, function, and dynamics in pancreatic β -cells. *Am. J. Physiol.-Endocrinol. Metab.* **2020**, *318*, E87–E101. [[CrossRef](#)] [[PubMed](#)]
45. Fedorov, A.; Beichel, R.; Kalpathy-Cramer, J.; Finet, J.; Fillion-Robin, J.C.; Pujol, S.; Bauer, C.; Jennings, D.; Fennessy, F.; Sonka, M.; et al. 3D Slicer as an image computing platform for the Quantitative Imaging Network. *Magn. Reson. Imaging* **2012**, *30*, 1323–1341. [[CrossRef](#)] [[PubMed](#)]
46. Mattei, G.; Giusti, S.; Ahluwalia, A. Design Criteria for Generating Physiologically Relevant In Vitro Models in Bioreactors. *Processes* **2014**, *2*, 548–569. [[CrossRef](#)]
47. Pias, S.C. How does oxygen diffuse from capillaries to tissue mitochondria? Barriers and pathways. *J. Physiol.* **2021**, *599*, 1769–1782. [[CrossRef](#)] [[PubMed](#)]
48. Pannala, V.R.; Camara, A.K.S.; Dash, R.K. Modeling the detailed kinetics of mitochondrial cytochrome *c* oxidase: Catalytic mechanism and nitric oxide inhibition. *J. Appl. Physiol.* **2016**, *121*, 1196–1207. [[CrossRef](#)]
49. Scandurra, F.M.; Gnaiger, E. Cell respiration under hypoxia: Facts and artefacts in mitochondrial oxygen kinetics. *Adv. Exp. Med. Biol.* **2010**, *662*, 7–25.
50. Suarez, R.K.; Lighton, J.R.; Brown, G.S.; Mathieu-Costello, O. Mitochondrial respiration in hummingbird flight muscles. *Proc. Natl. Acad. Sci. USA* **1991**, *88*, 4870–4873. [[CrossRef](#)]
51. Suarez, R.K. Upper limits to mass-specific metabolic rates. *Annu. Rev. Physiol.* **1996**, *58*, 583–605. [[CrossRef](#)]
52. Syromyatnikov, M.Y.; Gureev, A.P.; Vitkalova, I.Y.; Starkov, A.A.; Popov, V.N. Unique features of flight muscles mitochondria of honey bees (*Apis mellifera* L.). *Arch. Insect Biochem. Physiol.* **2019**, *102*, e21595. [[CrossRef](#)] [[PubMed](#)]
53. Gnaiger, E. Capacity of oxidative phosphorylation in human skeletal muscle. *Int. J. Biochem. Cell Biol.* **2009**, *41*, 1837–1845. [[CrossRef](#)] [[PubMed](#)]
54. Jacobs, R.A.; Lundby, C. Contextualizing the biological relevance of standardized high-resolution respirometry to assess mitochondrial function in permeabilized human skeletal muscle. *Acta Physiol. Oxf. Engl.* **2021**, *231*, e13625. [[CrossRef](#)] [[PubMed](#)]
55. Himmelblau, D.M. Diffusion of Dissolved Gases in Liquids. *Chem. Rev.* **1964**, *64*, 527–550. [[CrossRef](#)]
56. Longeville, S.; Stingaciu, L.-R. Hemoglobin diffusion and the dynamics of oxygen capture by red blood cells. *Sci. Rep.* **2017**, *7*, 10448. [[CrossRef](#)]
57. Moschandreou, T.E.; Ellis, C.G.; Goldman, D. Influence of tissue metabolism and capillary oxygen supply on arteriolar oxygen transport: A computational model. *Math. Biosci.* **2011**, *232*, 1–10. [[CrossRef](#)]
58. Radisic, M.; Deen, W.; Langer, R.; Vunjak-Novakovic, G. Mathematical model of oxygen distribution in engineered cardiac tissue with parallel channel array perfused with culture medium containing oxygen carriers. *Am. J. Physiol.-Heart Circ. Physiol.* **2005**, *288*, H1278–H1289. [[CrossRef](#)]
59. Hamon, M.; Hanada, S.; Fujii, T.; Sakai, Y. Direct oxygen supply with polydimethylsiloxane (PDMS) membranes induces a spontaneous organization of thick heterogeneous liver tissues from rat fetal liver cells in vitro. *Cell Transpl.* **2012**, *21*, 401–410. [[CrossRef](#)]
60. Morsiani, E.; Brogli, M.; Galavotti, D.; Bellini, T.; Ricci, D.; Pazzi, P.; Puviani, A.C. Long-Term Expression of Highly Differentiated Functions by Isolated Porcine Hepatocytes Perfused in a Radial-Flow Bioreactor. *Artif. Organs* **2001**, *25*, 740–748. [[CrossRef](#)]
61. Melendez-Ferro, M.; Rice, M.W.; Roberts, R.C.; Perez-Costas, E. An accurate method for the quantification of cytochrome C oxidase in tissue sections. *J. Neurosci. Methods* **2013**, *214*, 156–162. [[CrossRef](#)]
62. Buchwald, P. FEM-based oxygen consumption and cell viability models for avascular pancreatic islets. *Biol. Med.. Model* **2009**, *6*, 5. [[CrossRef](#)] [[PubMed](#)]
63. Suarez, R.K. Energy metabolism during insect flight: Biochemical design and physiological performance. *Physiol. Biochem. Zool.* **2000**, *73*, 765–771. [[CrossRef](#)] [[PubMed](#)]
64. Casey, T.M.; Arthur, P.G. Hibernation in Noncontracting Mammalian Cardiomyocytes. *Circulation* **2000**, *102*, 3124–3129. [[CrossRef](#)] [[PubMed](#)]
65. Peng, C.-A.; Palsson, B.O. Determination of specific oxygen uptake rates in human hematopoietic cultures and implications for bioreactor design. *Ann. Biomed. Eng.* **1996**, *24*, 373–381. [[CrossRef](#)] [[PubMed](#)]